

Tully-Fisher in the Zone of Avoidance. – Chapter 5.

Peculiar velocity of galaxies in the southern ZOA

Khaled Said

January 26, 2017

Abstract

In this chapter, we use the recently calibrated Tully-Fisher relation, deep NIR (J , H , and K_s -band) imaging, and high signal-to-noise HI data to derive distances and peculiar velocities for the largest and most homogeneous sample of inclined spiral galaxies hidden behind the dust and stellar density of our own Galaxy to date. This sample consists of ~ 300 galaxies covering the whole southern Zone of Avoidance ($|b| < 5^\circ$), out to redshift $z \sim 0.03$. We constructed the HI mass function using both $1/V_{max}$ and the two-dimensional stepwise maximum likelihood methods to correct for the Malmquist bias. All galaxies in the HIZOA survey that meet our selection criteria are included in the derivation of this HI mass function. The final parameters of the HI mass function are $\alpha = -1.30 \pm 0.05$, $\log(M_{HI}^*/M_\odot) = 9.97 \pm 0.04$, and $\phi^* = (5.2 \pm 0.8) \times 10^{-3} \text{ Mpc}^{-3}$. Comparisons of these parameters with values from the literature were performed. We present the compilation of TF based distances and peculiar velocities in the southern ZOA after applying all corrections. We mapped the velocity field to describe the motion of galaxies around the major large-scale structures, and the cosmography out to redshift $z \sim 0.03$. We found a clear positive peculiar velocities toward the direction of Hydra cluster and Shapley Supercluster. We also found strong positive peculiar velocities toward the direction and beyond Norma cluster. However, negative peculiar velocities were found in the Puppis region. We compared our velocity field to the 2MTF observations, 2MRS, and PSCz reconstructions. This final catalogue will be used in the future with the data from the northern ZOA and data from the 2MASS Tully-Fisher survey to provide the first all sky TF based distances and peculiar velocities survey.

1 Introduction

The Hubble law states that the recession velocity of a galaxy is directly proportional to its distance:

$$cz = H_0 r, \quad (1)$$

where cz is the recession velocity of that galaxy, r is its distance, and H_0 is the Hubble parameter, whose value remains as a source of ambiguity between the local measurements ($H_0 = 73.24 \pm 1.74 \text{ km s}^{-1} \text{ Mpc}^{-1}$; Riess et al. 2011, 2016; Efstathiou 2014) and the model-dependent measurements from the Planck temperature data ($H_0 = 67.8 \pm 0.9 \text{ km s}^{-1} \text{ Mpc}^{-1}$; Planck Collaboration et al. 2014a, 2016). However, we do not live in a perfectly smooth and homogeneous universe and most of the galaxies in our universe violate this law by having velocities above and below their expected Hubble velocities. Thus, a modification of the

Hubble law appeared as:

$$cz = H_0 r + \hat{r} \cdot [v(r) - v(0)], \quad (2)$$

where \hat{r} is the unit vector in the direction of that galaxy, $v(r)$ the galaxy peculiar velocity, and $v(0)$ is the observer peculiar velocity. This peculiar velocity arise as a result of the gravity of some over-density regions formed by the gravitational instability of the tiny perturbations in the uniform background. In the linear perturbation theory where the density fluctuation is small,

$$\delta(r) = \frac{\rho(r) - \rho_0}{\rho_0} < 1 \quad (3)$$

δ is the density contrast, ρ is the mass density field, and ρ_0 is the mean mass density, the peculiar velocities are directly proportional to the gravitational acceleration, via (Peebles, 1980, 1993; Strauss & Willick, 1995)

$$v(r) = \frac{H_0 f}{4\pi} \int d^3 r' \delta(r') \frac{r' - r}{|r' - r|^3}, \quad (4)$$

where astronomers always use km s^{-1} as the unit for distances which makes Hubble parameter in Eq. 4 equals unity, and f is the growth rate of the perturbations¹. Equation 4 shows that by measuring the peculiar velocities we can measure the fluctuation in the mass density and the growth of the perturbations.

These peculiar velocities can be measured statistically via the kinetic Sunyaev-Zeldovich effect (Sunyaev & Zeldovich, 1972) and redshift-space distortions (Kaiser, 1987) or individually for each galaxy via redshift independent distance indicator. In this chapter we focus only on the later method.

Two types of distance indicators can be used: (i) primary distance indicators which do not require calibration by another method, and (ii) secondary distance indicators, so-called because they require calibration via primary distance indicators. Typically Cepheid variable stars are used as the primary distance indicator, however beyond 20 Mpc they become too faint even with the Hubble Space Telescope, and a secondary indicator must be used. In the last few decades, the TF relation (Tully & Fisher, 1977) for spirals and the Faber-Jackson (FJ) relation (Faber & Jackson, 1976), the modified FJ relation (Dressler, 1987), and the Fundamental Plane (FP) relation (Djorgovski & Davis, 1987) for elliptical galaxies have been adopted as the workhorses for determining distances independent of the Hubble velocity relation. Only TF and FP relations have proven their ability to measure peculiar velocities for thousands of galaxies. Tully-Fisher (TF) analyses such as Cosmic Flows (Tully et al. 2009; Courtois et al. 2011) and the 2MASS (Jarrett et al., 2000) Tully-Fisher Survey (2MTF: Masters et al. 2008; Hong et al. 2013, 2014; Masters et al. 2014; Springob et al. 2016) or Fundamental Plane (FP) analyses such as 6dF (Magoulas et al. 2012; Campbell et al. 2014; Springob et al. 2014; Scrimgeour et al. 2016). Despite all these efforts, the overall bulk flow resulting from these studies can still not be fully reconciled with the dipole observed in the Cosmic Microwave Background (CMB), nor is there consistency about the volume which gives rise to the bulk flow.

One of the major limitations is the exclusion of some parts of the sky especially the ZOA (Kraan-Korteweg, 2005; Erdoğdu et al., 2006a; Loeb & Narayan, 2008) which is known to obscure major parts of dynamically important structures such as the Great Attractor (GA; Lynden-Bell et al. 1988; Woudt et al. 1999), the Local Void (LV; Tully & Fisher 1987; Kraan-Korteweg et al. 2008) and the recently discovered Vela Supercluster (VSCL;

¹The derivation of equation 4 from the continuity equation can be found in Peebles (1993) (section gravitational instability in chapter 5) or in Strauss & Willick (1995) (Section 2.2)

Kraan-Korteweg et al. 2017). Due to equation 4 these large scale structures will have a significant effect on the velocity field. Thus, the growth rate of the perturbations f will be also affected which is parametrized as a function of the cosmological density parameter Ω and the cosmological constant Λ , via Lahav et al. (1991)

$$f(\Omega, \Lambda)_{z=0} = \Omega^\gamma + \frac{\Lambda}{210H_0^2} \left(1 + \frac{\Omega}{2}\right) \quad (5)$$

where for flat Λ cold dark matter, $\gamma = 0.55$ (Wang & Steinhardt, 1998). Therefore, in addition to obtain constraints on cosmological parameters we can test other alternative models of gravity.

In this thesis we aim to measure distances and peculiar velocities to all inclined spiral galaxies in the southern ZoA. This will form the first part of the main project of providing the first ever truly all sky peculiar velocity survey by combining data from this thesis and data from the northern ZoA with the 2MTF data. By the end of this project we wish to give a definite answers to two main questions: (i) whether the bulk flow resulting from our all sky, large, and homogeneous sample is consistent with the predictions from the Λ cold dark matter model (Nusser & Davis, 2011; Turnbull et al., 2012; Hong et al., 2014; Scrimgeour et al., 2016) or we do not live in Λ cold dark matter universe and should test alternative models (Kashlinsky et al., 2008; Watkins et al., 2009; Feldman et al., 2010). (ii) whether the discrepancy between the dipole of the CMB which is a Doppler effect due to the Sun's motion (Hinshaw et al., 2009; Planck Collaboration et al., 2014b) and the Local Group peculiar velocity induced from our all sky, large, and homogeneous sample is because of the ZoA (Kraan-Korteweg & Lahav, 2000; Loeb & Narayan, 2008) or is it because of the depth of surveys Bilicki et al. (2011); Nusser et al. (2014) or both (Kraan-Korteweg et al., 2017).

This chapter is organized as follows: Section 2 we remind the reader of newly calibrated Tully-Fisher relation and its associated intrinsic scatter. In Section 3, we discuss both HI and NIR data in the ZoA which will be used in our calculation. Section 4 presents our method of calculating the distances and peculiar velocities. We also discuss our method for malmquist bias corrections which include the derivation of the HI mass function and the completeness of our sample in section 4. In section 4, we present the compilation of TF based distances and peculiar velocities in the southern ZOA after applying all corrections. We also present a qualitative analysis of the velocity field and the motion of galaxies around the major large-scale structures, and the cosmography out to redshift $z \sim 0.03$ in section 4. We summarize our results in Section 5.

2 Tully-Fisher Template Relation

Tully-Fisher relation is a correlation between the luminosity and the rotation of spiral galaxies Tully & Fisher (1977). Given that, luminosity depends on the distance of galaxy, whereas rotational velocity does not, this correlation can be used to infer galaxy distances. The other application for this relation is to study galaxy formation because rotational velocity is related to the amount of galactic dark matter or the dark matter halo, while luminosity is not. The later application is out of the focus of this thesis and we will only focus on the first application. However, as any secondary distance indicator, TF relation requires a calibration before using it as a standard tool to measure distances independent of redshift. In chapter 2, we re-calibrate the Tully-Fisher relation using the isophotal magnitudes in J , H , and K_s -band of 888 galaxies (Said et al., 2015). The reason of re-calibrating these

relations is that most of the already existing relations used the total magnitude which can not be measured in the ZoA because of dust extinction and high stellar density. While the sample used for the calibration contains only galaxies from high galactic latitude, all parameters and methods should be consistent with the sample used for the measurements of TF based distances and peculiar velocities. After applying all corrections for magnitudes and H I 21-cm linewidths, the final isophotal TF relations have the form:

$$M_J - 5 \log h = -20.951 - 9.261(\log W - 2.5), \quad (6a)$$

$$M_H - 5 \log h = -21.682 - 9.288(\log W - 2.5), \quad (6b)$$

$$M_{K_s} - 5 \log h = -21.861 - 10.369(\log W - 2.5), \quad (6c)$$

and after very careful considerations of all sources of uncertainty in the above relations we found that the intrinsic scatter of these relations have the form of:

$$\epsilon_{int,J} = 0.46 - 0.90(\log W - 2.5), \quad (7a)$$

$$\epsilon_{int,H} = 0.47 - 0.94(\log W - 2.5), \quad (7b)$$

$$\epsilon_{int,K_s} = 0.46 - 0.83(\log W - 2.5). \quad (7c)$$

Equations 6 & 7 will be used as a benchmark or standard tool in measuring distances and peculiar velocities of galaxies in our TF distance based sample, which is introduced in the coming section.

3 ZOA DATA

The required two sets of raw data to calculate the TF based distances and peculiar velocities are: (i) H I 21-cm observations of spiral galaxies in the ZOA from which to extract the redshift and the rotational velocity, and (ii) follow-up deep NIR imaging of the H I sources to measure the apparent magnitude of each galaxy. In the coming subsections, we present the data used and the corrections made for each data set to be consistent with the data used for the calibration of the template relations.

3.1 H I data

The first data set which is the 21 cm H I-line spectra of inclined, $(b/a)^\circ < 0.5$, spiral galaxies selected from the HIZOA survey (Staveley-Smith et al., 2016) was achieved by re-observing these galaxies using the narrow band on Parkes radio telescope to obtain better velocity resolution (Said et al., 2016). The average signal-to-noise ratio for this H I survey was 14.7 which is adequate for TF studies and five different types of line-widths are measured, which are:

1. W_{P20} : the linewidth at 20% of the peak flux—rms,
2. W_{M50} : the linewidth at 50% of the mean flux,
3. W_{P50} : the linewidth at 50% of the peak flux—rms,
4. W_{F50} : the linewidth at 50% of the peak flux—rms, measured with a polynomial fit to both sides of the profile,

Table 1: Velocity width instrumental correction parameters (Springob et al., 2005).

(Δv) (km s ⁻¹)	Smoothing	$\lambda_1(\Delta v)$	$\lambda_2(\Delta v)$	$\lambda'_2(\Delta v)$	$\lambda_3(\Delta v)$
< 5	H	0.005	-0.468	0.785	0.395
5-11	H	$0.04\Delta v - 0.18$	$0.05\Delta v - 0.72$	$-0.03\Delta v + 0.92$	$0.02\Delta v + 0.28$
> 11	H	0.227	-0.1523	0.623	0.533
< 5	B	0.020	-0.4705	0.820	0.430
5-11	B	$0.05\Delta v - 0.24$	$0.04\Delta v - 0.67$	$0.02\Delta v + 0.72$	$0.06\Delta v - 0.12$
> 11	B	0.332	-0.2323	0.940	0.802

5. W_{2P50} , the linewidth at 50% of the peak flux–rms measured at each of the two peaks.

full presentation of this data set can be found in chapter 3 of this thesis. To be consistent with the calibration method, we used the same linewidth, which is W_{F50} and the same equation given by Springob et al. (2007) to correct it for the inclination.

$$W = \left[\frac{w_{F50} - \Delta_s}{1 + z} - \Delta_t \right] \frac{1}{\sin i} \quad (8)$$

where Δ_t is the effect of turbulent motion and Δ_s is the instrumental correction. For the the effect of turbulent motion, $\Delta_t = 6.5 \text{ km s}^{-1}$ is used, and for the instrumental correction

$$\Delta_s = 2\Delta v \lambda \quad (9)$$

is used (Springob et al., 2005). The parameter λ is a piece-wise defined function of signal-to-noise ratio (SNR) and channel separation:

$$\lambda = \lambda_1(\Delta v) \quad \log(\text{SNR}) < 0.6, \quad (10a)$$

$$\lambda = \lambda_2(\Delta v) + \lambda'_2(\Delta v) \log(\text{SNR}) \quad 0.6 < \log(\text{SNR}) \leq 1.1, \quad (10b)$$

$$\lambda = \lambda_3(\Delta v) \quad \log(\text{SNR}) > 1.1. \quad (10c)$$

Table 1 shows the values of λ as given in (Springob et al., 2005). The inclination i is derived from the J -band ellipticity $\epsilon_J = 1 - (b/a)_J$ via

$$\cos^2 i = \frac{(1 - \epsilon)^2 - q_0^2}{1 - q_0^2} \quad (11)$$

following Giovanelli et al. (1997). The parameter $(a/b)_J$ is the J -band axial ratio fit to the 3σ isophote (the isophote which corresponds to a surface brightness ~ 3 times the background noise). The J -band axial ratio $(b/a)_J$ is the best tracer of the inclination, it suffers less than H , and K_s -bands from the effect of the bulge if the 3σ isophote is close to the center (Masters et al., 2003).

Additionally, the peculiar velocities need to be in the CMB frame. I transform the heliocentric velocity v_{hel} to v_{CMB} using the model given by Fixsen et al. (1996):

$$v_{\text{CMB}} = v_{\text{hel}} + v_{\text{apex}} [\sin b \sin b_{\text{abex}} + \cos b \cos b_{\text{abex}} \cos(l - l_{\text{abex}})] \quad (12)$$

where $v_{\text{apex}} = 371.0 \text{ km s}^{-1}$, $l_{\text{abex}} = 264^\circ 14$, and $b_{\text{abex}} = 48^\circ 26$ are the velocity and Galactic coordinates of the apex vector describing the relative motion of the Sun with respect to the CMB.

3.2 NIR data

The second data set is the systematic deep NIR observations of spiral galaxies at low Galactic latitudes. Said et al. (2016) presents a deep near-infrared (NIR; J , H , and K_s bands) photometric catalogue of sources from the Parkes HI Zone of Avoidance (HIZOA) survey. Observations were conducted using the Japanese Infrared Survey Facility (IRSF), a 1.4-m telescope situated at the South African Astronomical Observatory site in Sutherland and resulted in over a thousand galaxies. Full representation of this data set can be found in chapter 4. Again, the correction for the absolute magnitude of the galaxy is calculated from the observed apparent magnitude in a consistent way with the template relations as:

$$M_{\text{corr}} - 5\log h = m_{\text{obs}} - A_X - I_X - k_X - 5\log v_{\text{CMB}} - 15, \quad (13)$$

where A_X , I_X , and k_X are a correction for extinction due to dust in our galaxy, a correction for extinction internal to the galaxy itself, and a cosmological k -correction, respectively.

For galactic extinction we used the correction provided in Riad et al. (2010). We used the correction for internal extinction from Said et al. (2015). For the k -correction we used the same procedure used by Masters et al. (2008) & Said et al. (2015). The correction model for the axial ratio b/a due to dust extinction derived by Said et al. (2015) is used. Additional correction for the morphological type is applied using the equations derived by Said et al. (2015).

4 TF based distances and peculiar velocities

With the above mentioned three ingredients in hand, the absolute magnitude can be derived using the template relation given the rotational velocity. The distance to each galaxy can then be calculated independent of the redshift using the distance modulus.

4.1 Calculating the logarithmic distance ratio

Following Hong et al. (2014) & Springob et al. (2016), we work with the logarithmic distance ratio instead of the linear peculiar velocities because the distance errors are log-normal. We define the logarithmic distance ratios to have the form of:

$$\log(d_z/d_{TF}^*) = \frac{-\Delta M}{5}, \quad (14)$$

where $\Delta M = M_{\text{obs}} - M(W)$. Figure 1 shows the distribution of ΔM in the J , H , and K_s -band. The dashed lines in the three panels are the three template TF relations in J , H , and K_s bands (equations 6). The dark shaded area shows the intrinsic scatter in the TF relations (equations 7) and the light shaded area denotes three times the intrinsic scatter, $\pm 3\epsilon_{\text{int}}$. In Figure 1 we cut out from our sample only outliers galaxies. We define outliers as any galaxy with large linewidth or magnitude error that results in more than $3\epsilon_{\text{int}}$ deviation from the TF relation.

d_{TF}^* is the distance to the galaxy derived from the TF relation and not corrected for selection bias. Figure 2 shows a histogram of the distribution of the logarithmic distance ratio derived by combining all three wavebands J , H , and K_s uncorrected for the selection bias.

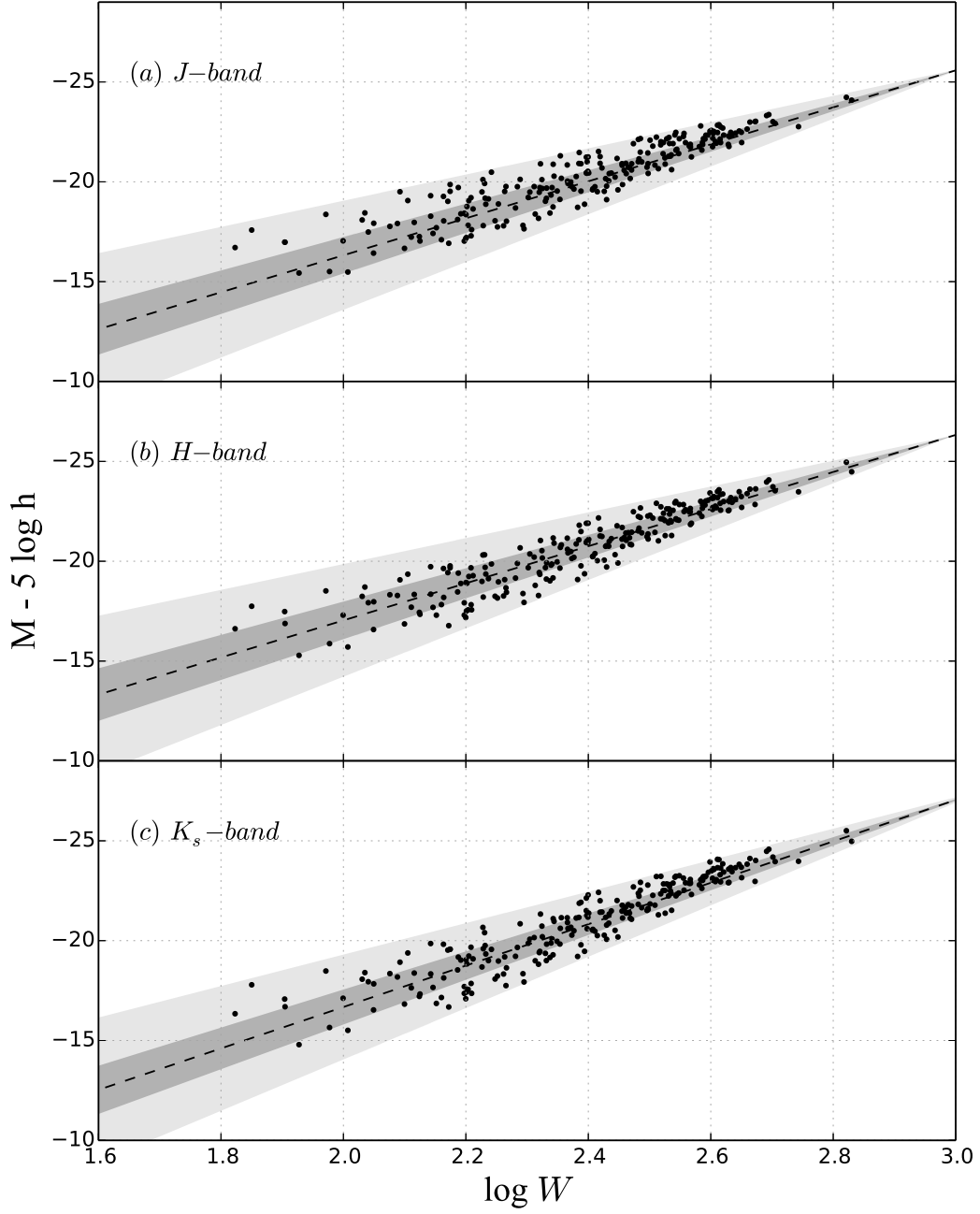


Figure 1: Tully-Fisher relation for galaxies in the ZoA. Absolute magnitude of our sample derived from IRSF isophotal magnitude in the J -band as a function of rotation width. The dashed line denotes the TF relations in J , H , and K_s -band (equations 6). The dark shaded area shows the intrinsic scatter (equations 7) and the light shaded area represents a three times the TF intrinsic scatter ($\pm 3\epsilon_{int}$).

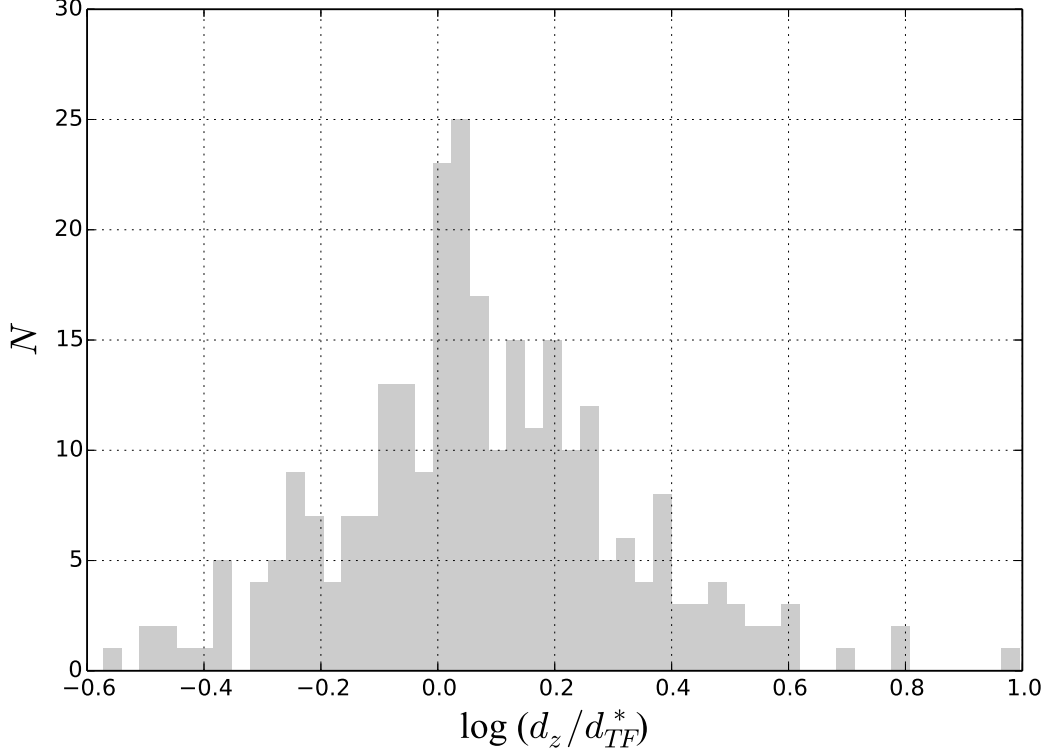


Figure 2: The distribution of the uncorrected logarithmic distance ratio $\log(d_z/d_{TF}^*)$ derived by combining all three wavebands J , H , and K_s .

We used the propagation of errors to calculate the error on the logarithmic distance ratios $\log(d_z/d_{TF}^*)$.

$$\sigma_{\log(d_z/d_{TF}^*)} = \frac{\sigma_{\Delta M}}{5} \quad (15a)$$

$$\sigma_{\Delta M}^2 = \sigma_M^2 + \sigma_{M(W)}^2 \quad (15b)$$

$$\sigma_M^2 = \sigma_{obs}^2 + \left(\frac{5}{v_{CMB} \ln 10}\right)^2 \sigma_{v_{CMB}}^2 \quad (15c)$$

$$\sigma_W^2 = \left(\frac{1}{1+z}\right)^2 \sigma_{W_{F50}}^2 + \left(W \frac{\cos i}{\sin i}\right)^2 \sigma_i^2 \quad (15d)$$

$$\sigma_i^2 = \left(\frac{1-\epsilon}{1-q_0^2 \cos i \sin i}\right)^2 \sigma_\epsilon^2 \quad (15e)$$

$$\sigma_{M(W)}^2 = \left(\frac{b}{W \ln 10}\right)^2 \sigma_W^2 + \epsilon_{int}^2. \quad (15f)$$

Figure 3 shows the distribution of the error of the logarithmic distance ratios $\log(d_z/d_{TF}^*)$ uncorrected for the selection bias also derived by combining data from all three wavebands J , H , and K_s .

4.2 Malmquist bias Correction

The logarithmic distance ratios $\log(d_z/d_{TF}^*)$ derived in the previous subsection and its associated errors are subject to Malmquist bias and careful corrections are needed before using

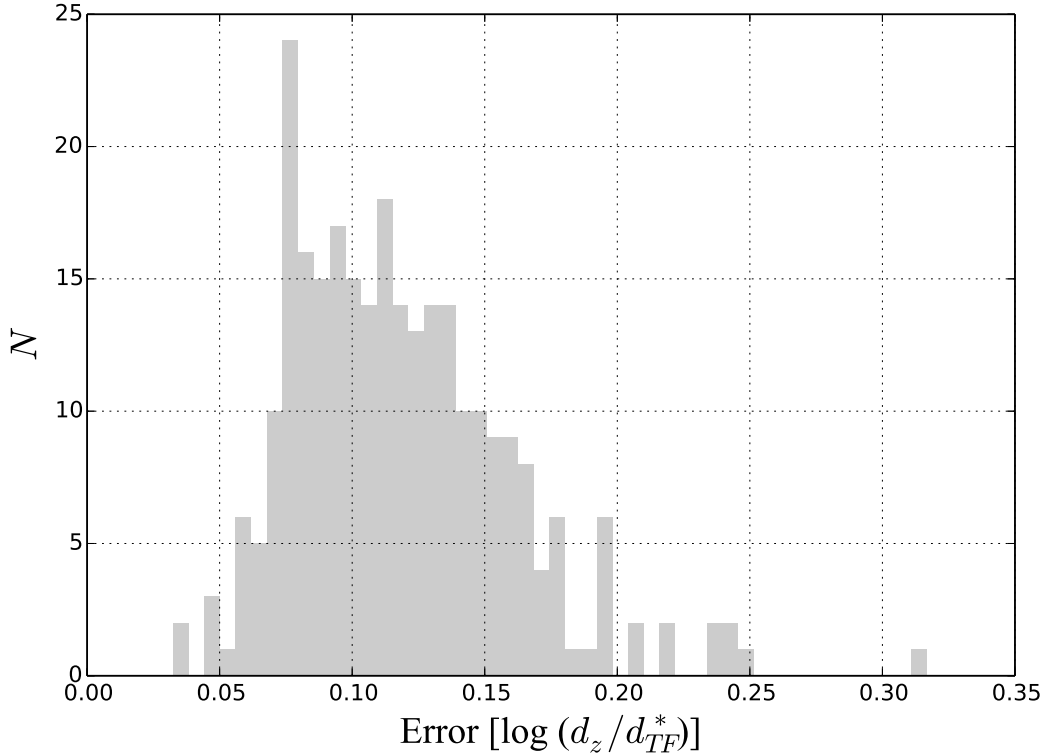


Figure 3: The distribution of the uncorrected error of the logarithmic distance ratios $\log(d_z/d_{TF}^*)$ derived by combining all three J , H , and K_s wavebands.

them for any cosmological applications. There are two types of Malmquist bias: Inhomogeneous Malmquist bias and homogeneous Malmquist bias. Working with redshift space instead of real space makes the inhomogeneous Malmquist bias negligible (Strauss & Willick, 1995).

In this section we will deal only with the homogeneous Malmquist bias. This type of selection bias is a consequence of two effects: (1) volume effect and (2) selection effect (see, Springob et al. 2016 for more details about both effects). We adopt the same procedure used in the 2MTF, which is achieved by constructing the HI mass function instead of the luminosity function and calculate the fraction of the target sample that is included in our final TF sample for a given flux bin instead of magnitude bin.

4.2.1 HI mass function

We use the HI mass function because our sample is derived from the HI survey, HIZOA. We derive the HI mass function for all galaxies in the HIZOA survey that meet our selection criteria. HIZOA survey have three completeness limits: (1) flux limit, (2) Mean flux density limit and (3) the hybrid limit (see Table. 4 in Staveley-Smith et al 2015). We used the V/V_{max} -test (Schmidt, 1968) to measure the uniformity of galaxy distribution within the survey volume for each limit. The mean of the statistic V/V_{max} was 0.407 ± 0.009 , 0.454 ± 0.009 , and 0.344 ± 0.008 for flux limit, Mean flux density limit, and the hybrid limit, respectively. The expected mean V/V_{max} value for a uniform sample is 0.5. Values smaller than 0.5 means that the sample is more incomplete at larger distances than at lower distances. For that reason, we choose to work with the Mean flux density limit which gives the closest value to 0.5.

We derived the HIMF with both $1/V_{max}$ (Schmidt, 1968) and the two-dimensional step-wise maximum likelihood (2DSWML: Loveday 2000; Zwaan et al. 2003, 2005) methods.

$1/V_{max}$ method has been widely used because of its simplicity. The number density of galaxies is simply calculated by summing the $1/V_{max}$ in bins of H I masses as follows:

$$\phi(M_{HI})_j = \frac{1}{\Delta M_{HI}} \sum \frac{1}{V_{max,i}}, \quad (16)$$

where $\phi(M_{HI})_j$ is the number density of galaxies in bin $j = 1, 2, \dots, N_{M_{HI}}$ and $N_{M_{HI}}$ is the number of bins in H I masses. $V_{max,i}$ is the maximum volume of galaxy $i = 1, 2, \dots, N_g$ and calculated as

$$V_{max,i} = \frac{4\pi f_{sky}}{3} \left\{ \frac{M_{HI,i}}{2.356 \times 10^5 S_{lim} W_{50,i}} \right\}^{3/2} \quad (17)$$

where the mean flux density $S_{lim} = 22$ mJy represent the completeness limit of the HIZOA survey (Donley et al., 2005; Staveley-Smith et al., 2016), f_{sky} is the fraction of the sky covered by the survey, and $M_{HI,i}$ is given by,

$$M_{HI,i} = 2.356 \times 10^5 D_i^2 F_{HI,i}, \quad (18)$$

where D_i is the distance in megaparsecs and $F_{HI,i}$ is the flux integral.

We fit a Schechter function (Schechter, 1976) of the form:

$$\Phi(M_{HI}) = \ln 10 \phi^* \left(\frac{M_{HI}}{M_*} \right)^{\alpha+1} e^{-\frac{M_{HI}}{M_*}}, \quad (19)$$

to the derived H I mass function. The best fit parameters are $\alpha = -1.35 \pm 0.04$, $\log(M_{HI}^*/M_\odot) = 9.94 \pm 0.24$, and $\phi^* = (10.65 \pm 4.11) \times 10^{-3} \text{ Mpc}^{-3}$.

The main problem of the $1/V_{max}$ method is its sensitivity to large scale structures because it assumes that galaxies are uniformly distributed in space. The HIZOA survey covers many large scale structures such as the great attractor and the local void, which means that these structures will affect each bin in different ways.

In contrast, the 2DSWML method is independent of any density fluctuations. This method find the maximum likelihood solutions for the number density of galaxies ϕ_{jk} as a function of H I mass and velocity width by iterating from an initial guess as:

$$\phi_{jk} = \frac{\sum_{i=1}^{N_g} \delta(M_i - M_j, W_i - W_k)}{\sum_{i=1}^{N_g} \frac{H_{ijk} \Delta M \Delta W}{\sum_{l=1}^{N_M} \sum_{m=1}^{N_W} \phi_{ilm} H_{ilm} \Delta M \Delta W}}, \quad (20)$$

where δ_{ijk} is a function equals 1 if a galaxy i belongs to H I mass bin j and velocity width bin k , and equals 0 otherwise, and the function H_{ijk} equals the fraction of bin jk available to a galaxy i (Zwaan et al., 2003).

Equation 20 can be interpreted in many different ways. The denominator for example, present the effective volume available to galaxies in bin jk , and can be modified to find the effective volume available to each galaxy as in Zwaan et al. (2005). Marginalizing Eq. 20 over velocity width W gives the H I mass function (Martin et al., 2010; Jones et al., 2016) while marginalizing over the H I mass M_{HI} gives the velocity width function (Papastergis et al., 2011). In this chapter I will focus only on the HIMF.

We used Eq. 20 to evaluate the effective volume available to each single galaxy that meet the selection criteria of the TF analysis after applying the completeness function of

the HIZOA survey. Figure 4 shows the galaxy density distribution in the $M_{HI}W_{50}$ -plane colour coded by the reciprocal of the effective volume available to each galaxy in logarithmic scale.

We then marginalized ϕ_{jk} over the velocity width to calculate the HIMF as:

$$\phi_j = \sum_{k=1}^{N_W} \phi_{jk} \Delta W \quad (21)$$

Figure 5 shows the result of this process. The circles present the number space density in HI mass bins, the solid line is the best fit Schechter function of the form presented in Eq. 19, and the error bars are the Poisson errors. The final parameters of the HI mass function are $\alpha = -1.30 \pm 0.05$, $\log(M_{HI}^*/M_\odot) = 9.97 \pm 0.04$, and $\phi^* = (5.2 \pm 0.8) \times 10^{-3} \text{ Mpc}^{-3}$. The normalization is not needed for the Malmquist bias correction. These parameters are printed on Fig. 5 itself. For comparison, we show Zwaan et al. (2003) results as a dotted line and Martin et al. (2010) as a dashed line. The faint end slope derived here agrees, within the uncertainty, with both Zwaan et al. (2003) and Martin et al. (2010) but not with Zwaan et al. (2005) which gives a much steeper slope. Again the knee of the HI mass function derived here agrees with Martin et al. (2010) results but not with either Zwaan et al. (2003) or Zwaan et al. (2005). The difference between $1/V_{max}$ and 2DSWML parameters confirms Martin et al. (2010) results that the effect of the large scale structure correction is very small on $\log(M_{HI}^*/M_\odot)$ but are 10% on α and 30% on ϕ^* . For the rest of this Chapter we will only use the 2DSWML results.

4.2.2 Completeness

Completeness is the fraction of the target sample, all galaxies in HIZOA that meet our selection, included into our final sample for a given flux bin. Figure 6 shows histograms of the target sample and the final observed sample. We used the HIZOA flux limit in this figure.

We calculate the fraction as a function of flux bin and fit a quadratic function to the scatter. We used some smoothing to fit this function to avoid unreal scatter. Figure 7 shows the fraction of the target sample included into our final TF sample.

4.2.3 Apply the correction

For each galaxy we derived the probability distribution of the uncorrected logarithmic distance ratio assuming a normal distribution with 1σ of the error. For each logarithmic distance we weight the probability by the reciprocal of the completeness integrated over the HI mass function, evaluated at the logarithmic distance in question. Then we fit a Gaussian to the new probability distribution to get the corrected logarithmic distance and the corrected logarithmic error. The corrected logarithmic distances and errors are shown in Figs. 8 & 9, respectively.

4.3 Velocity Field in the ZoA

In this subsection, we work with the Super Galactic longitude and latitude (SGL, SGB) and Super Galactic Cartesian coordinates (SGX, SGY, SGZ) transferred from the Galactic longitude and latitude (l, b) plus distance via de Vaucouleurs et al. (1976) & Tully (1988).

We divided our sample into three slices of SGZ to distinguish between the motion of galaxies around the approximated positions of nearby large-scale structure. Figures 10, 11,

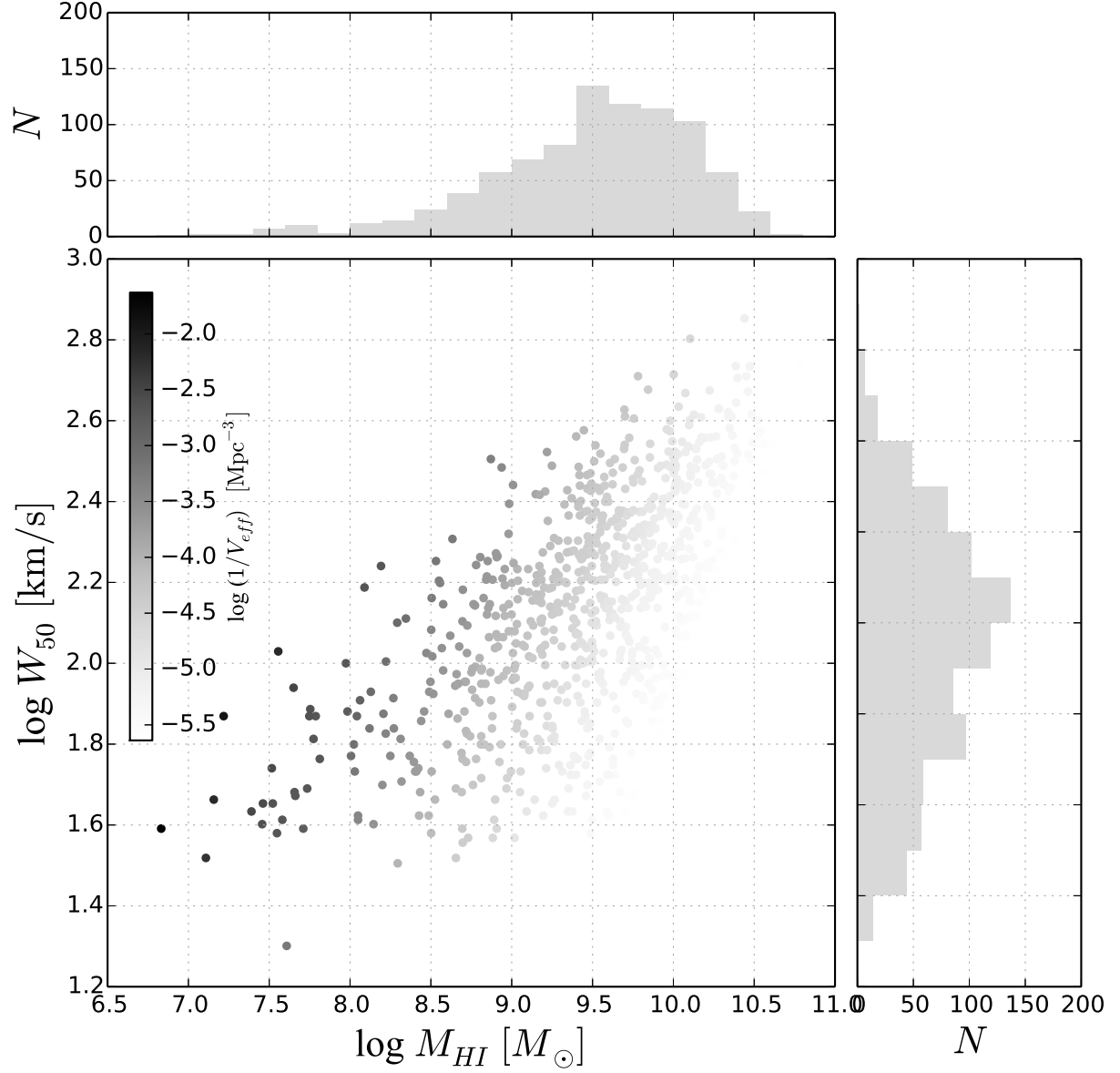


Figure 4: Galaxy density distribution in the $M_{HI}W_{50}$ -plane. Each dot present a galaxy color coded by the reciprocal of the effective volume available to it in logarithmic scale. This effective volume is calculated via the two-dimensional stepwise maximum likelihood method.

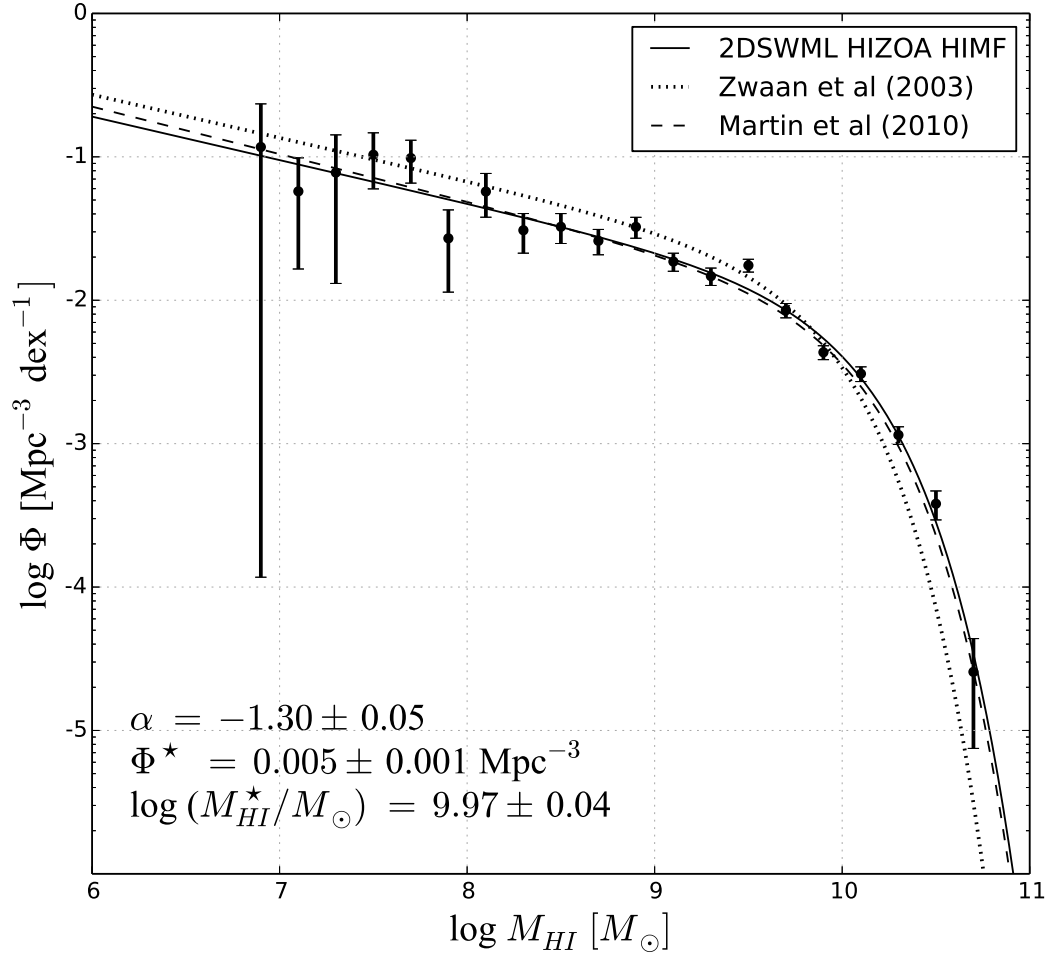


Figure 5: HIZOA HI mass function derived via the two-dimensional stepwise maximum likelihood method. For comparison, we added the HI mass function of HIPASS BGC (dotted line; Zwaan et al. 2003) and ALFALFA 40% (dashed line; Martin et al. 2010).

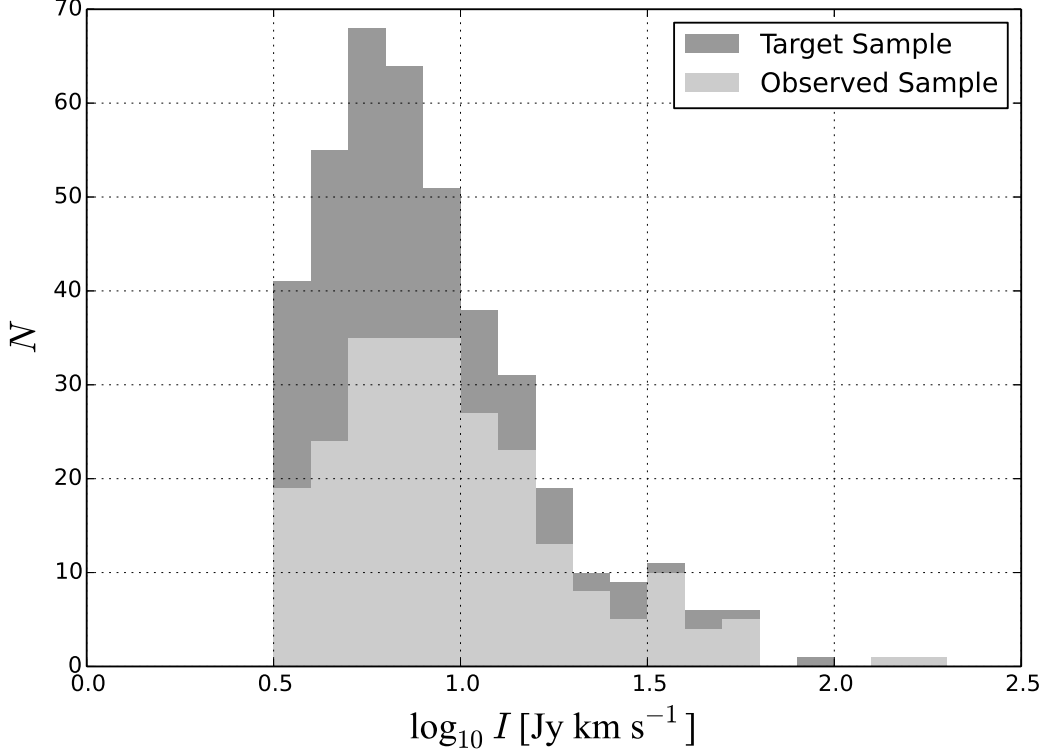


Figure 6: The fraction of the target sample that included into our final TF based distance sample for a given flux bin.

and 12 present the velocity field in slices of $SGZ < -20h^{-1}$ Mpc, $20 < SGZ < -20h^{-1}$ Mpc, and $SGZ > 20h^{-1}$ Mpc, respectively. In all three figures the velocity field is given in the logarithmic distance ratios unit $\log(d_z/d_{TF}^*)$. Red color present the positive peculiar velocity, which is away from the center of the $SGX - SGY$ plane, and blue color present the negative peculiar velocity, which toward the center of the $SGX - SGY$ plane. In these figures we show the velocity field, smoothed with a Gaussian kernel of radius $4 h^{-1}$ Mpc as in Carrick et al. (2015) & Springob et al. (2016), in the logarithmic distance ratios unit $\log(d_z/d_{TF}^*)$.

In Figure 10 the approximated positions of Hydra cluster, and Puppis region are:

$$(l, b, cz, SGX, SGY, SGZ) = (270.0^\circ, 26.0^\circ, 3500 \text{ km s}^{-1}, -28.41, 23.73, -28.42),$$

and $(l, b, cz, SGX, SGY, SGZ) = (245.0^\circ, 0.0^\circ, 2500 \text{ km s}^{-1}, -10.09, 3.50, -31.57)$, respectively. There is a clear indication of positive peculiar velocity toward the negative SGX and the positive SGY which is the direction of Hydra cluster and Shapley Supercluster. In contrast, we see a lot of negative peculiar velocities in the Puppis region which is toward the center of the figure, the $SGX - SGY$ plane.

Figure 11 shows the velocity field in the $20 < SGZ < -20h^{-1}$ Mpc slice which contains the Norma cluster:

$(l, b, cz, SGX, SGY, SGZ) = (325.255^\circ, -7.1279^\circ, 4707 \text{ km s}^{-1}, -61.69, -8.68, 7.63)$. Very strong and clear infall toward the negative SGX and SGY which is the direction of Norma cluster is shown. This infall does not stop at the Norma position but continue in the same direction toward the negative SGX and SGY . On the positive side of SGY plane we see more negative peculiar velocities, which point toward the center of the $SGX - SGY$ plane, than the negative side of the SGY plane.

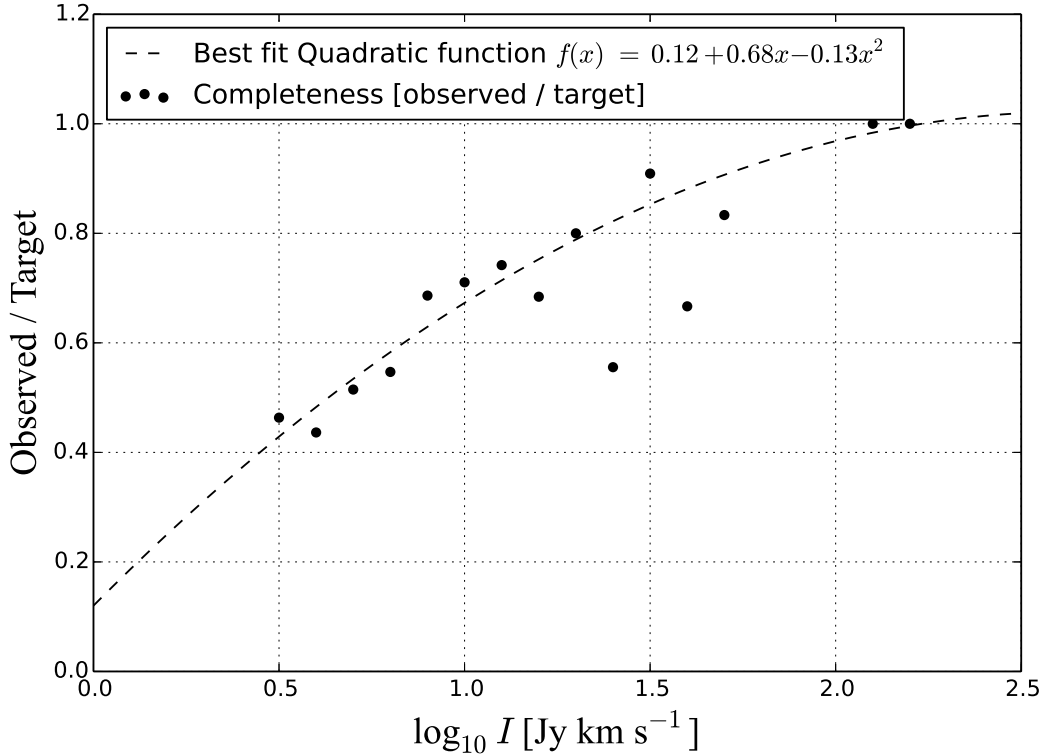


Figure 7: Quadratic function represent the completeness of our final TF sample. We smoothed our data before fitting this function to avoid the outliers.

Figure 12 shows the velocity field in the $SGZ > 20h^{-1}$ Mpc slice. In this slice we see a strong positive peculiar velocities in all direction and we do not see any negative peculiar velocities.

Although, the area that our sample covers is small, we still can compare with other velocity fields observations and reconstructions. Figure 4 by Springob et al. (2016) showed the velocity field as derived by 2MTF (Hong et al., 2014), the 2MASS Redshift Survey (2MRS; Erdođdu et al. 2006b), and the IRAS Point Source Catalog Redshift Survey (PSCz; Branchini et al. 1999) in three slices of SGZ similar to Figs. 10, 11, and 12. The first slice (Fig. 10; $SGZ < -20h^{-1}$ Mpc) agrees with the 2MTF observations which is the first panel of Fig. 4 by Springob et al. (2016) but does not agree with either 2MRS or PSCz reconstructions, which are panels 2 and 4, respectively. The second slice (Fig. 11; $20 < SGZ < -20h^{-1}$), 2MTF observations, 2MRS, and PSCz reconstructions all agree on the infall into Norma cluster (l, b, cz, SGX, SGY, SGZ) = (325.255°, -7.1279°, 4707 km s⁻¹, -61.69, -8.68, 7.63). The third slice (Fig. 12; $SGZ > 20h^{-1}$ Mpc) agrees only with the 2MRS reconstructions which also shows a positive peculiar velocity in all direction and hardly shows any negative velocities. Even the signal for negative velocities in the 2MRS reconstructions are very weak. On the other hand, our results disagree with both 2MTF observations and PSCz reconstructions.

5 Summary

In this chapter we measured the distances and peculiar velocities of inclined spiral galaxies hidden behind our own Milky Way. We started by reminding the reader of the calibrated

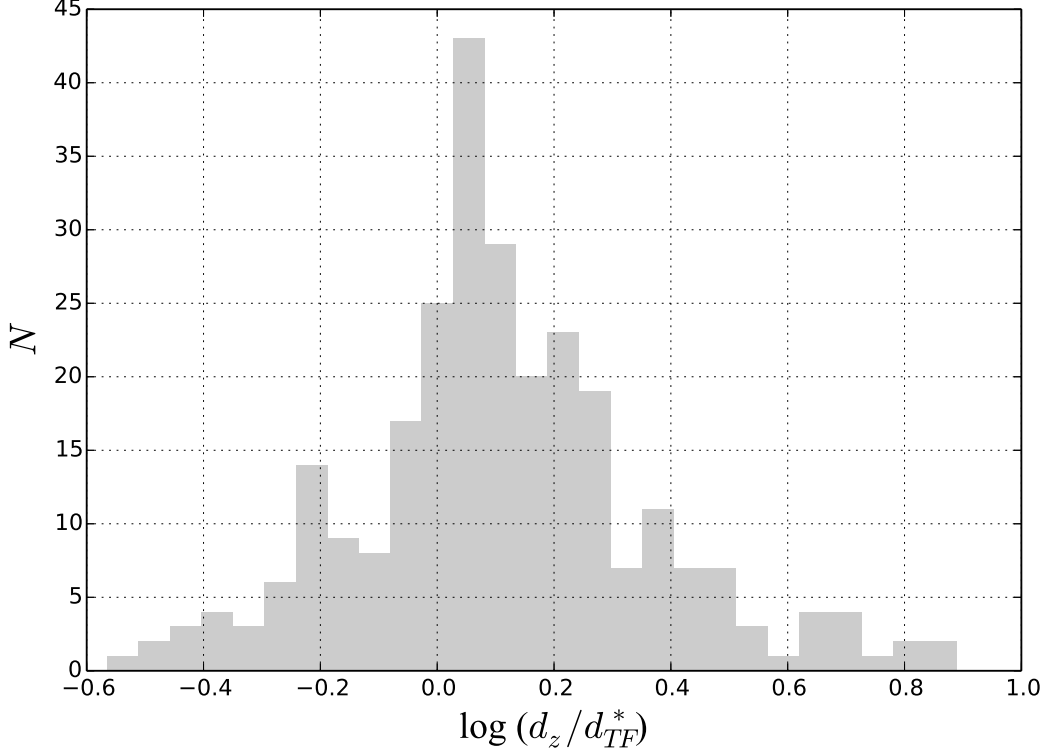


Figure 8: The distribution of the logarithmic distance ratio $\log(d_z/d_{TF}^*)$ by combining all three wavebands J , H , and K_s after applying the Malmquist bias correction.

Tully-Fisher relations in the J , H , and K_s bands. Then we presented our method on how to prepare and correct the raw data to be used in the calculation of the distances and peculiar velocities in the Zone of Avoidance. In the process of calculating the TF based distances and peculiar velocities we choose to work with the logarithmic distance ratio instead of the linear peculiar velocities because the distance errors are log-normal. We also choose to work with redshift space instead of real space to avoid the inhomogeneous Malmquist bias. However, to correct for the homogeneous Malmquist bias we constructed HI mass function using both $1/V_{max}$ and the two-dimensional stepwise maximum likelihood methods. All galaxies in the HIZOA survey that meet our selection criteria are included in the derivation of this HI mass function. The final parameters of the HI mass function are $\alpha = -1.30 \pm 0.05$, $\log(M_{HI}^*/M_\odot) = 9.97 \pm 0.04$, and $\phi^* = (5.2 \pm 0.8) \times 10^{-3} \text{ Mpc}^{-3}$. Comparisons of these parameters with values from the literature were performed. We found that the faint end slope derived here agrees, within the uncertainty, with both HIPASS BGC and ALFALFA. However, the knee of the HI mass function derived here agrees with the ALFALFA results but not with the HIPASS results. We also derived the completeness as the fraction of the target sample included into our final sample for a given flux bin. Using both HI mass function and the completeness function we corrected the logarithmic distance ratios $\log(d_z/d_{TF}^*)$. We then used the corrected logarithmic distance ratios to derive the velocity field in slices of SGZ . In each slice of SGZ we tested the motion of galaxies around the approximated positions of features of large scale structures such as Hydra cluster;

$$(l, b, cz, SGX, SGY, SGZ) = (270.0^\circ, 26.0^\circ, 3500 \text{ km s}^{-1}, -28.41, 23.73, -28.42),$$

Puppis region:

$$(l, b, cz, SGX, SGY, SGZ) = (245.0^\circ, 0.0^\circ, 2500 \text{ km s}^{-1}, -10.09, 3.50, -31.57),$$

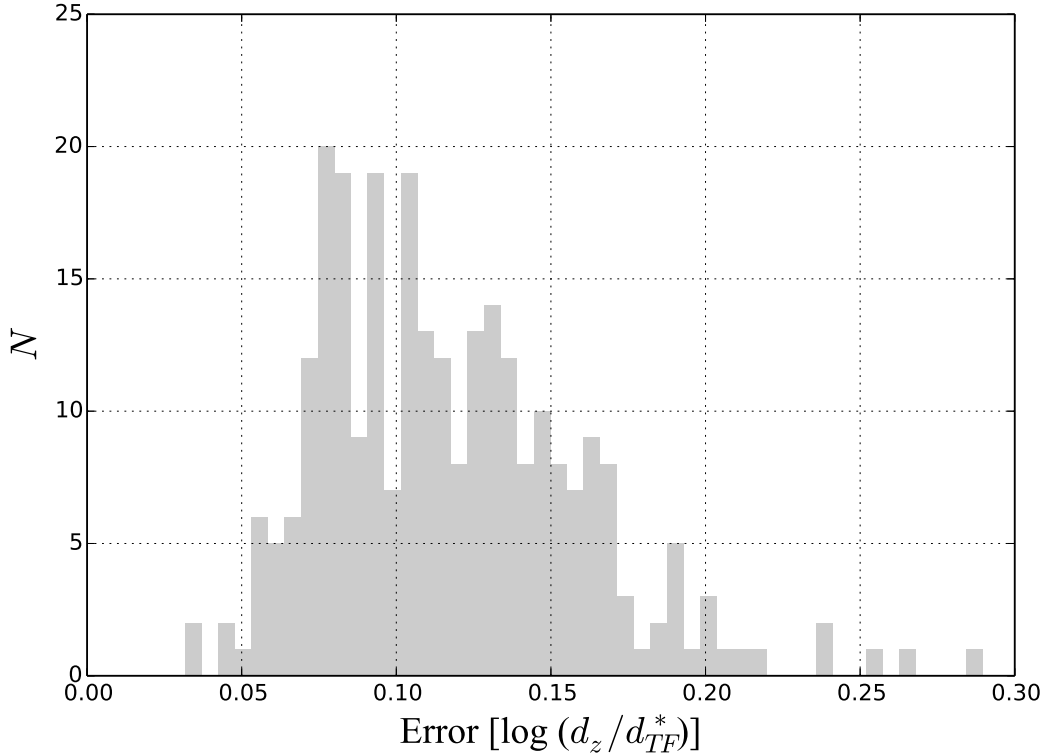


Figure 9: The distribution of the error of the logarithmic distance ratio $\log(d_z/d_{TF}^*)$ by combining all three wavebands J , H , and K_s after applying the Malmquist bias correction.

and the Norma cluster

$$(l, b, cz, SGX, SGY, SGZ) = (325.255^\circ, -7.1279^\circ, 4707 \text{ km s}^{-1}, -61.69, -8.68, 7.63).$$

We found a clear positive peculiar velocities toward the direction of Hydra cluster and Shapley Supercluster. We also found strong positive peculiar velocities toward the direction and beyond Norma cluster. In contrast, we found that galaxies in the Puppis region to have negative peculiar velocities toward the center of the $SGX - SGY$ plane.

We compared our velocity field to 2MTF observation (Hong et al., 2014; Springob et al., 2016), 2MRS (Erdoğdu et al., 2006b), and PSCz (Branchini et al., 1999) reconstructions. The velocity field derived in this thesis agrees, at low redshift, with 2MTF observations but disagree with both 2MRS, and PSCz reconstructions. However, all four velocity fields agrees on the infall into the Norma cluster. At high redshift our results agrees only with 2MRS which also show positive velocities in all directions. In contrast, our results at high redshift disagree with both 2MTF and PSCz.

This sample presents the first of three parts of our final sample. A new collaboration led by Prof. Kraan-Korteweg started last year to obtain deep and high velocity-resolution HI data. These narrow-band observations started this year using the Nançay Radio Telescope, France. This collaboration will provide the HI 21-cm data set and UKIDSS will be used to provide the NIR data set. The next step will be to extend this work by combining it with the 2MTF survey and provide the first ever truly all-sky peculiar velocity survey **2MTF+**. We will use this survey to compare the dipole of the CMB which is a Doppler effect due to the Sun's motion (Hinshaw et al., 2009; Planck Collaboration et al., 2014b) with the LG peculiar velocity induced from our sample. Such analysis used to be limited due to the lack of observations in the ZoA (Loeb & Narayan, 2008). We will also measure the bulk flow

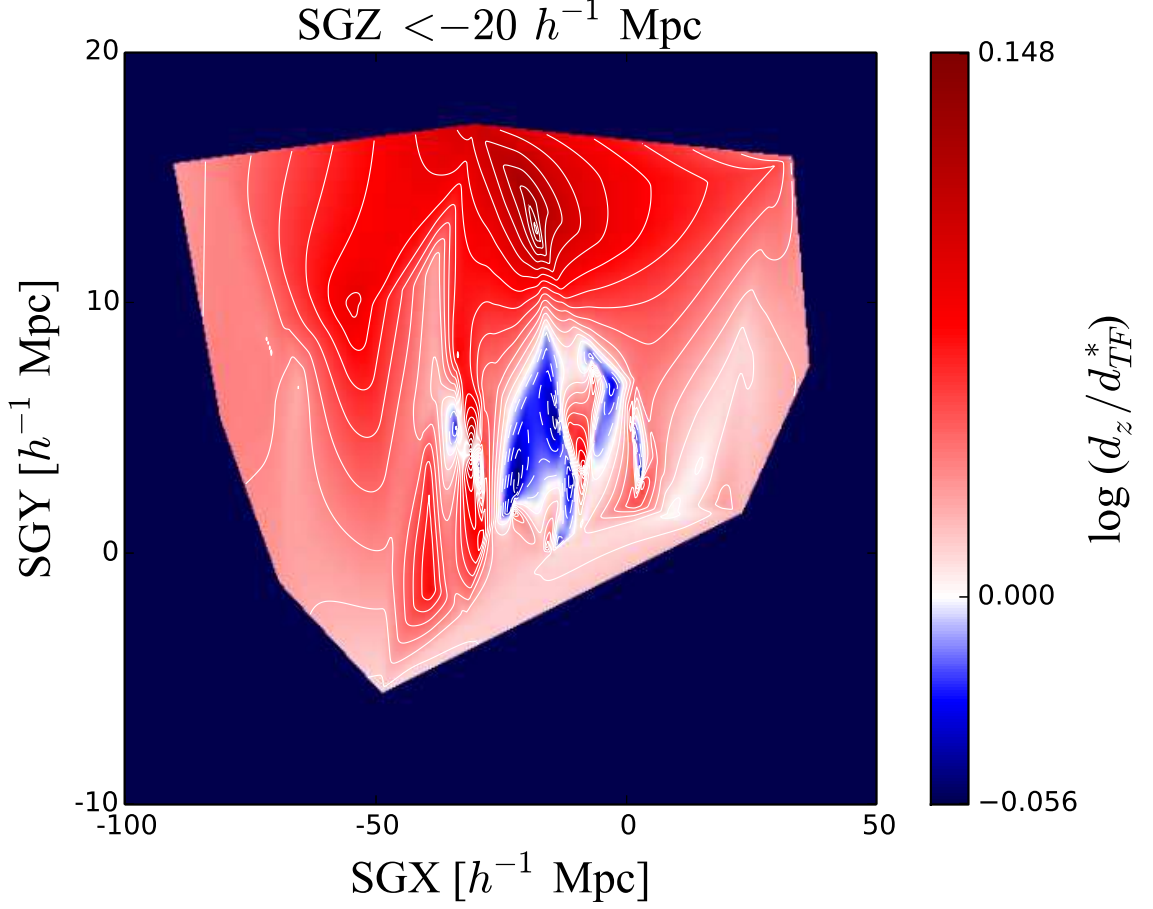


Figure 10: The velocity field (smoothed with a Gaussian kernel of radius $4 h^{-1}$ Mpc) in the logarithmic distance ratios unit $\log(d_z/d_{TF}^*)$ of galaxies in the $SGZ < -20h^{-1}$ Mpc slice. Red color present the positive peculiar velocity, which is away from the center of the $SGX - SGY$ plane, and blue color present the negative peculiar velocity, which toward the center of the $SGX - SGY$ plane. The solid contour $\log(d_z/d_{TF}^*) = 0.01$, the dashed contour $\log(d_z/d_{TF}^*) = -0.01$, and the successive contours thereafter increase toward the maximum $\log(d_z/d_{TF}^*)$ and $-\log(d_z/d_{TF}^*)$ for solid and dashed contour, respectively. The approximated positions of Hydra cluster is $(l, b, cz, SGX, SGY, SGZ) = (270.0^\circ, 26.0^\circ, 3500 \text{ km s}^{-1}, -28.41, 23.73, -28.42)$ and Puppis region is $(l, b, cz, SGX, SGY, SGZ) = (245.0^\circ, 0.0^\circ, 2500 \text{ km s}^{-1}, -10.09, 3.50, -31.57)$. Clear indication of positive peculiar velocity toward the direction of Hydra cluster. This positive peculiar velocity is also in the direction of Shapley Supercluster, which is beyond the limits of our coordinates. A lot of negative peculiar velocity in the Puppis region which point toward the center of the $SGX - SGY$ plane.

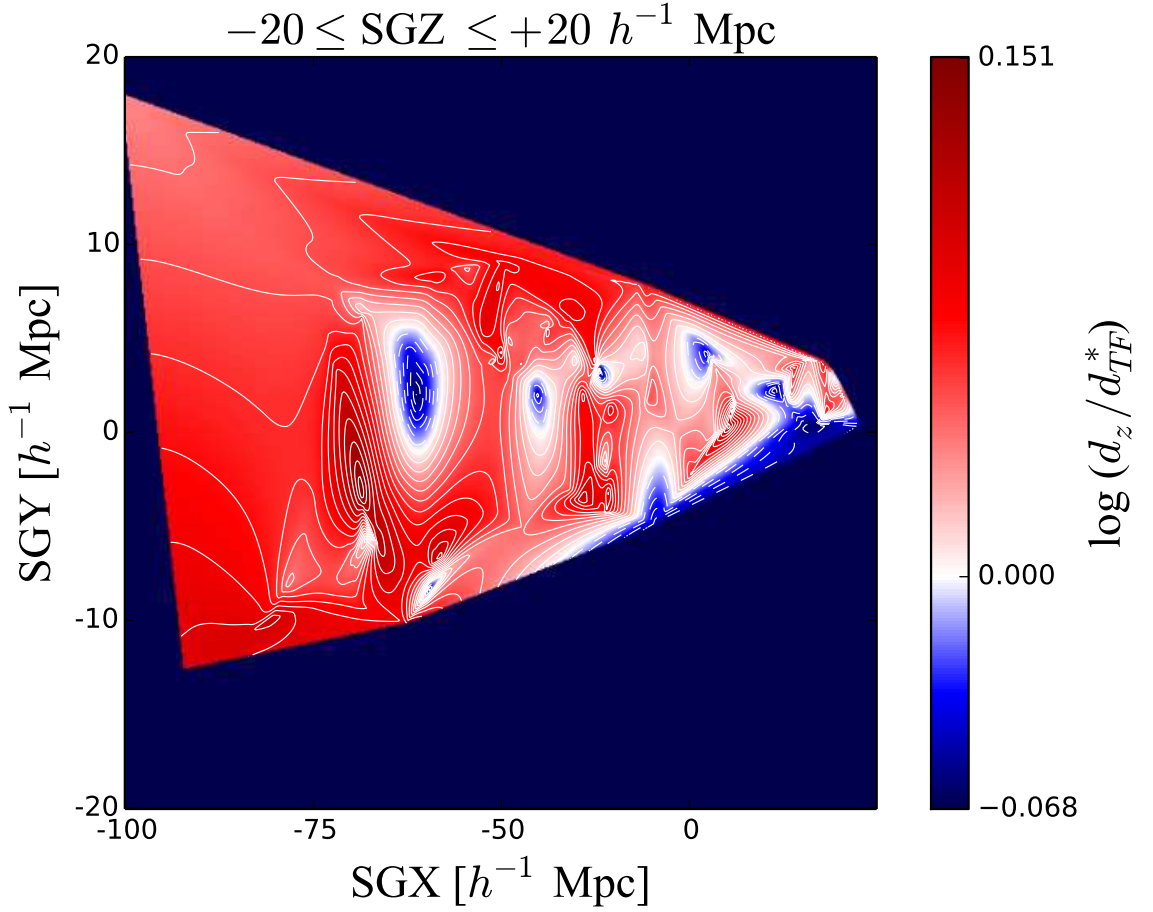


Figure 11: The velocity field in the logarithmic distance ratios unit $\log(d_z/d_{TF}^*)$ of galaxies in the $20 < SGZ < -20 h^{-1}$ Mpc slice. Smoothing, colors, and contours are the same as in Fig. 10. The approximated position of the Norma cluster is $(l, b, cz, SGX, SGY, SGZ) = (325.255^\circ, -7.1279^\circ, 4707 \text{ km s}^{-1}, -61.69, -8.68, 7.63)$. Strong positive peculiar velocities toward the direction of the Norma cluster and beyond is shown.

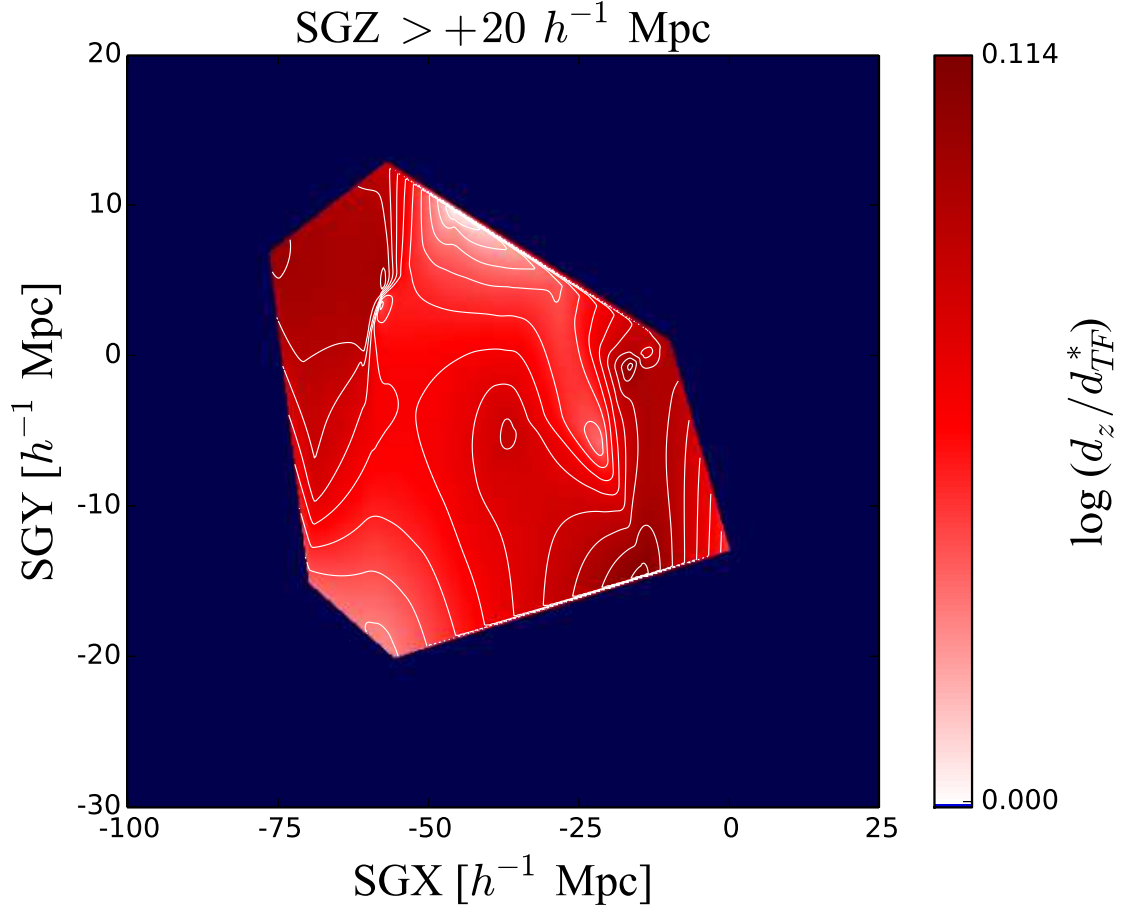


Figure 12: The velocity field in the logarithmic distance ratios unit $\log(d_z/d_{TF}^*)$ of galaxies in the $SGZ > 20h^{-1} \text{ Mpc}$ slice. Smoothing, colors, and contours are the same as in Fig. 10. Strong positive peculiar velocities in all direction are shown.

resulting from our all sky sample and compare it with the predictions from the Λ cold dark matter model.

References

- Bilicki M., Chodorowski M., Jarrett T., Mamon G. A., 2011, *ApJ* , 741, 31
- Branchini E. et al., 1999, *MNRAS* , 308, 1
- Campbell L. A. et al., 2014, *MNRAS* , 443, 1231
- Carrick J., Turnbull S. J., Lavaux G., Hudson M. J., 2015, *MNRAS* , 450, 317
- Courtois H. M., Tully R. B., Héraudeau P., 2011, *MNRAS* , 415, 1935
- de Vaucouleurs G., de Vaucouleurs A., Corwin Jr. H. G., 1976, Second reference catalogue of bright galaxies. Containing information on 4,364 galaxies with references to papers published between 1964 and 1975.
- Djorgovski S., Davis M., 1987, *ApJ* , 313, 59
- Donley J. L. et al., 2005, *AJ* , 129, 220
- Dressler A., 1987, *ApJ* , 317, 1
- Efstathiou G., 2014, *MNRAS* , 440, 1138
- Erdoğdu P. et al., 2006a, *MNRAS* , 368, 1515
- Erdoğdu P. et al., 2006b, *MNRAS* , 373, 45
- Faber S. M., Jackson R. E., 1976, *ApJ* , 204, 668
- Feldman H. A., Watkins R., Hudson M. J., 2010, *MNRAS* , 407, 2328
- Fixsen D. J., Cheng E. S., Gales J. M., Mather J. C., Shafer R. A., Wright E. L., 1996, *ApJ* , 473, 576
- Giovanelli R., Haynes M. P., Herter T., Vogt N. P., da Costa L. N., Freudling W., Salzer J. J., Wegner G., 1997, *AJ* , 113, 53
- Hinshaw G. et al., 2009, *ApJS* , 180, 225
- Hong T. et al., 2014, *MNRAS* , 445, 402
- Hong T. et al., 2013, *MNRAS* , 432, 1178
- Jarrett T. H., Chester T., Cutri R., Schneider S., Skrutskie M., Huchra J. P., 2000, *AJ* , 119, 2498
- Jones M. G., Papastergis E., Haynes M. P., Giovanelli R., 2016, *MNRAS* , 457, 4393
- Kaiser N., 1987, *MNRAS* , 227, 1
- Kashlinsky A., Atrio-Barandela F., Kocevski D., Ebeling H., 2008, *ApJL* , 686, L49
- Kraan-Korteweg R. C., 2005.
- Kraan-Korteweg R. C., Cluver M. E., Bilicki M., Jarrett T. H., Colless M., Elagali A., Böhringer H., Chon G., 2017, *MNRAS* , 466, L29
- Kraan-Korteweg R. C., Lahav O., 2000, *A&A Rev.*, 10, 211
- Kraan-Korteweg R. C., Shafi N., Koribalski B. S., Staveley-Smith L., Buckland P., Henning P. A., Fairall A. P., 2008. p. 13
- Lahav O., Lilje P. B., Primack J. R., Rees M. J., 1991, *MNRAS* , 251, 128
- Loeb A., Narayan R., 2008, *MNRAS* , 386, 2221
- Loveday J., 2000, *MNRAS* , 312, 557
- Lynden-Bell D., Faber S. M., Burstein D., Davies R. L., Dressler A., Terlevich R. J., Wegner G., 1988, *ApJ* , 326, 19
- Magoulas C. et al., 2012, *MNRAS* , 427, 245
- Martin A. M., Papastergis E., Giovanelli R., Haynes M. P., Springob C. M., Stierwalt S., 2010, *ApJ* , 723, 1359

Masters K. L., Crook A., Hong T., Jarrett T. H., Koribalski B. S., Macri L., Springob C. M.,
 Staveley-Smith L., 2014, MNRAS , 443, 1044
 Masters K. L., Giovanelli R., Haynes M. P., 2003, AJ , 126, 158
 Masters K. L., Springob C. M., Huchra J. P., 2008, AJ , 135, 1738
 Nusser A., Davis M., 2011, ApJ , 736, 93
 Nusser A., Davis M., Branchini E., 2014, ApJ , 788, 157
 Papastergis E., Martin A. M., Giovanelli R., Haynes M. P., 2011, ApJ , 739, 38
 Peebles P. J. E., 1980, The large-scale structure of the universe
 Peebles P. J. E., 1993, Principles of Physical Cosmology
 Planck Collaboration et al., 2014a, A&A, 571, A16
 Planck Collaboration et al., 2016, A&A, 594, A13
 Planck Collaboration et al., 2014b, A&A, 571, A27
 Riad I. F., Kraan-Korteweg R. C., Woudt P. A., 2010, MNRAS , 401, 924
 Riess A. G. et al., 2011, ApJ , 730, 119
 Riess A. G. et al., 2016, ApJ , 826, 56
 Said K., Kraan-Korteweg R. C., Jarrett T. H., 2015, MNRAS , 447, 1618
 Said K., Kraan-Korteweg R. C., Jarrett T. H., Staveley-Smith L., Williams W. L., 2016,
 MNRAS , 462, 3386
 Said K., Kraan-Korteweg R. C., Staveley-Smith L., Williams W. L., Jarrett T. H., Springob
 C. M., 2016, MNRAS , 457, 2366
 Schechter P., 1976, ApJ , 203, 297
 Schmidt M., 1968, ApJ , 151, 393
 Scrimgeour M. I. et al., 2016, MNRAS , 455, 386
 Springob C. M., Haynes M. P., Giovanelli R., Kent B. R., 2005, ApJS , 160, 149
 Springob C. M. et al., 2016, MNRAS , 456, 1886
 Springob C. M. et al., 2014, MNRAS , 445, 2677
 Springob C. M., Masters K. L., Haynes M. P., Giovanelli R., Marinoni C., 2007, ApJS , 172,
 599
 Staveley-Smith L., Kraan-Korteweg R. C., Schröder A. C., Henning P. A., Koribalski B. S.,
 Stewart I. M., Heald G., 2016, AJ , 151, 52
 Strauss M. A., Willick J. A., 1995, Phys. Rep., 261, 271
 Sunyaev R. A., Zeldovich Y. B., 1972, Comments on Astrophysics and Space Physics, 4, 173
 Tully R. B., 1988, Nearby galaxies catalog
 Tully R. B., Fisher J. R., 1977, A&A, 54, 661
 Tully R. B., Fisher J. R., 1987, Atlas of Nearby Galaxies
 Tully R. B., Rizzi L., Shaya E. J., Courtois H. M., Makarov D. I., Jacobs B. A., 2009, AJ ,
 138, 323
 Turnbull S. J., Hudson M. J., Feldman H. A., Hicken M., Kirshner R. P., Watkins R., 2012,
 MNRAS , 420, 447
 Wang L., Steinhardt P. J., 1998, ApJ , 508, 483
 Watkins R., Feldman H. A., Hudson M. J., 2009, MNRAS , 392, 743
 Woudt P. A., Kraan-Korteweg R. C., Fairall A. P., 1999, A&A, 352, 39
 Zwaan M. A., Meyer M. J., Staveley-Smith L., Webster R. L., 2005, MNRAS , 359, L30
 Zwaan M. A. et al., 2003, AJ , 125, 2842